Available online at www.sciencedirect.com
SCIENCE DIRECT®
Physica D 209 (2005) 245–259
PHYSICA D
www.elsevier.com/locate/physd

On undercompressive shocks in constrained two-layer flows

T.M. Segin[a,1], B.S. Tilley[b], L. Kondic[a,*]

[a] *Department of Mathematical Sciences, Center for Applied Mathematics and Statistics, New Jersey Institute of Technology, Newark, NJ 07102, USA*
[b] *Franklin W. Olin College of Engineering, Needham, MA 02492, USA*

Available online 25 July 2005

Abstract

We consider the countercurrent flow of two incompressible immiscible viscous fluids in an inclined channel. The lower fluid is denser than the upper fluid, making this configuration relevant to air-water systems. Flow is driven by an imposed pressure gradient and gravity. From a lubrication approximation based on the ratio of the channel height to the downstream disturbance wavelength, we derive a nonlinear system of evolution equations that govern the interfacial shape separating the two fluids and the leading-order pressure. This system includes the physical effects of advection, capillarity, inertia and hydrostatic pressure. Our interest is to compare the dynamics of the solutions under different flow constraints. In particular, we compare the dynamics when the liquid volumetric flow rate and the downstream pressure drop are held fixed to the case when the gas volumetric flow rate and the interfacial height at ends of the channel are held fixed. In both of these systems, Lax shocks, undercompressive shocks and rarefaction waves are investigated. Through a numerical verification, we find that the dynamics of both scenarios are different, resulting in unsteady interfacial profiles for flows driven by fixed liquid flow rate and pressure drop.

Keywords: Two-fluid flow; Undercompressive shocks

1. Introduction

Understanding of liquid films is important in many physical systems such as cooling systems, coating processes and biological applications. Examples of their importance include oil and gas flow through subsea tiebacks (Moritis [19]), condensate flow in gas wells (Duenckel [9]), the flow of hydrocarbons in furnace tubes or liquid in cooling systems of nuclear installations, and in the on-chip cooling of micro-electromechanical (MEMS) devices (Pettigrew et al. [20]). Two-phase gas–liquid flows can also be important in some space operations such as the design and operation of spacecraft environmental systems, storage and transfer of cryogenic fluids (Duckler et al. [10], Bousman et al. [5]).

* Corresponding author.
E-mail addresses: tms3@njit.edu (T.M. Segin), burt.tilley@olin.edu (B.S. Tilley), kondic@njit.edu (L. Kondic).
[1] Present address: Department of Chemical and Materials Engineering, University of Alberta, Edmonton, AB, Canada T6G 2G6.

0167-2789/$ – see front matter © 2005 Elsevier B.V. All rights reserved.
doi:10.1016/j.physd.2005.06.030

Two-phase cocurrent (both phases flow in the same direction) down-flow of air and water was extensively studied by Kouris and Tsamopoulos [16] in a host of geometries ranging from model arrangements to single vertical constricted tubes. They found that the difference in viscosity of the two fluids induces an interfacial velocity, which is directly responsible for the transition from chaotic interactions obtained for near unit viscosity ratios μ, to well organized wave trains for large values of μ. For the case of two-layer flow the initiating mechanism for the long-wave instability is richer than one for the single-layer (due to viscosity and density stratification). Linear stability of two superposed layers of fluids was first studied by Yih [26] for the plane Couette–Poiseuille flow in a horizontal channel. Using a long-wave assumption, he showed that the interface was susceptible to the instability due to the viscosity stratification. Tilley et al. [24,25] investigated the influence of the channel thickness and the average interfacial height on the stability of two-layer superposed fluid flow, and identified the mechanisms for linear and nonlinear stability in the long-wave limit where the flow rate of each layer is prescribed.

The problem of the two-fluid flow which can flow cocurrently (the fluids flow in the same direction) or countercurrently (fluids flow in opposite directions) is partially motivated by the phenomenon called *flooding*, found in countercurrent flows. This term is used to describe various aspects of the transition from countercurrent to cocurrent flow adverse to gravity, as the pressure gradient is increased. Example of flooding phenomenon considered here is large interfacial deformations of the liquid that prevents the flow of gas. Flooding has been investigated extensively both phenomenologically (Chang [7], Fowler and Lisseter [12]) and experimentally (see Bankoff and Lee [1] and the references therein; Dukler and Smith [11]), but the criteria for onset of flooding is still an open question. During the transition from countercurrent to cocurrent upstream flow a whole range of waves is observed, from possibly chaotic small-amplitude ones to large-amplitude waves that impede the flow of the top fluid.

A related problem arises when single phase thin film flows under gravity along a heated plate in such a way that thermocapillary forces act against gravity. These films arise in thin coating flows and are of great technical and scientific interest. Recently, it has been discovered that the interfacial dynamics of these films includes the development of undercompressive shocks. There is also a growing amount of theoretical work indicating that undercompressive shocks are observed in other physical systems. For example, Kluwick et al. [15] find these waves in modified Korteweg-de-Vries-Burgers equation which describes the evolution of weakly nonlinear concentration waves in suspensions of particles in fluids. Another example is undercompressive shocks in water alternating gas recovery that according to Marchesin and Plohr [18] have a great practical potential for improving the efficiency.

The first indication of this more complicated interfacial dynamics, which includes undercompressive shocks, comes from the comparison of two series of experiments: Ludviksson and Lightfoot [17] and Cazabat and coworker [6]. Experiment in [17] shows that for thicker Marangoni films balanced with gravity, no bump or capillary ridge is present near the contact line and the front is relatively stable. In contrast, [6] reports a well-formed fingering instability at the leading edge of a climbing film which develops within minutes of applying a vertical temperature gradient. This "contradiction" between results of experiments of [6,17] inspired new analytical and experimental studies (Bertozzi et al. [3,4]), in which the formation of a very large capillary ridge is observed. The ridge continues to broaden as it advances up the plate. Despite the large capillary ridge, the contact line remains stable; [3] emphasizes that undercompressive shock plays a key role in preventing the contact line from fingering (i.e. breaking up into rivulets). Solutions with undercompressive shocks are known to arise in equations with nonconvex fluxes and combined diffusive and dispersive effects. Schneemilch and Cazabat [21,22] showed experimentally that a novel undercompressive shock (for which characteristics enter the shock on one side and leave on the other) theory for infinite films and substrates could be applied to real systems of finite dimensions.

Single-layer driven thin films are examples of an open system, in which the pressure at the interface is determined by a constant ambient pressure and capillarity. The air plays a passive role in the interfacial evolution. In the two-layer system, however, pressure acts to ensure that the total mass of both fluids is conserved, and plays an active role in the interfacial dynamics. Hence, global constraints on the pressure or on the flow parameters themselves play a significant role in the interfacial evolution.

Almost all models discussed above were investigated under the assumption of constant-flux boundary conditions. An alternative boundary condition is to fix the pressure drop over the length of the channel. If the assumption of

passive upper layer is relaxed and two-fluid flow considered, then one can expect that the difference between the constant flow rate and constant pressure drop régimes in gas phase will be more pronounced. We note that in experiments and applications it is very difficult to maintain a constant flow rate, especially when upper fluid is a gas. Therefore, there is a strong motivation for considering constant liquid flow rate and pressure drop régime, and that is the main topic of this paper. From our earlier work (Segin et al. [23]), a two-fluid system driven by a constant gas volumetric flow rate and gravity, assuming that the average interfacial height remain constant in time, is found to have the same interfacial phenomenon (undercompressive shocks) seen in the single-layer, thermally driven case described above. In this work, we compare these results with the ones obtained using conditions of a fixed liquid volumetric flow rate (or equivalently a fixed liquid Reynolds number) and a fixed pressure drop. We find that linear stability of a flat interfacial solution remains the same, but unlike the traveling-wave dynamics found in our previous study, the average interfacial height varies in time as the spatial interfacial deflections evolve.

The structure of this paper is as follows. In Section 2 we formulate the problem, discuss the assumptions under which our model is valid, and present system of the highly nonlinear evolution equation and the leading order pressure gradient equation. Section 3 discusses the implemented boundary conditions for the evolution equation and solutions for both cases under consideration. We find numerically that the structure of the interfacial profile for given system parameters (ratio of densities, dynamical viscosities etc.) involves the Lax (classical) shock, double shock (Lax and undercompressive), and combination of rarefaction wave with undercompressive shock. However, the dynamics in both cases is quite different.

2. Formulation and governing equations

Consider the flow of two viscous incompressible fluids in a channel of height d and length L (Fig. 1), where $\mathbf{n}$ is the unit normal pointing from phase 1 into phase 2, and $\mathbf{t}$ is the unit tangent vector at the interface. The equations that govern this system are continuity and Navier–Stokes (asterisks denote dimensional variables):

$$\bar{\nabla} \cdot \mathbf{u}^{*(i)} = 0,$$

$$\rho_i^* \left(\frac{\partial \mathbf{u}^{*(i)}}{\partial t^*} + \mathbf{u}^{*(i)} \cdot \bar{\nabla} \mathbf{u}^{*(i)} \right) = -\bar{\nabla} p^{*(i)} + \rho_i^* \mathbf{g} + \mu_i^* \bar{\nabla}^2 \mathbf{u}^{*(i)}.$$

The superscript (i) on the dependent variables correspond to $i = 1$, lower fluid and $i = 2$, upper fluid, respectively, with corresponding densities ρ_i^*, dynamic viscosities μ_i^* and pressures $p^{*(i)}$, $\mathbf{g} = g(\sin\beta, -\cos\beta)$ denotes the gravitational acceleration vector, where β is the inclination angle ($\beta = \pi/2$ in Fig. 1). The velocities $\mathbf{u}^{*(i)} = (u^{*(i)}, w^{*(i)})$ satisfy the boundary conditions on the channel walls: $\mathbf{u}^{*(1)} = 0$ at z^*=0 and $\mathbf{u}^{*(2)} = 0$ at $z^* = d$, as well as the balance of normal stress, balance of tangential stress, continuity of normal and tangential components of velocity and kinematic condition at $z^* = h^*(x^*, t^*)$:

$$[\mathbf{n} \cdot \mathbf{T}^* \cdot \mathbf{n}] = \sigma^* \kappa^*, \qquad [\mathbf{t} \cdot \mathbf{T}^* \cdot \mathbf{n}] = 0, \qquad [\mathbf{u}^* \cdot \mathbf{n}] = 0, \qquad [\mathbf{u}^* \cdot \mathbf{t}] = 0, \qquad h_{t^*}^* + u^* h_{x^*}^* - w^* = 0, \tag{1}$$

where the jump $[f]$ of the quantity f across the interface is denoted by $[f] = f^{(2)} - f^{(1)}$. T^* denotes the stress tensor, σ^* is the surface tension between the two fluids, and κ^* is twice the mean curvature of the interface, given by:

$$\kappa^* = -h_{x^*x^*}^* (1 + h_{x^*}^{*2})^{-3/2}.$$

We scale lengths by d, time by $\nu_1^*/\mathrm{d}g$, densities by ρ_1^* and velocities by $d^2 g/\nu_1^*$, where ν_1^* is the kinematic viscosity of the lower fluid. That determines the pressure scale as $\rho_1^* \mathrm{d}g$. Thus, we obtain:

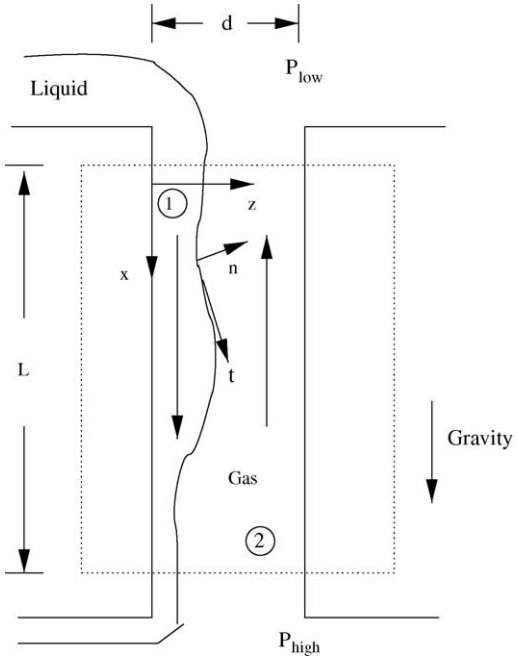

Fig. 1. Basic outline of the problem of interest. The plate on the left is coated by a liquid driven by gravity, pointing down (here the inclination angle $\beta = \pi/2$), while the gas is driven by an adverse pressure drop (higher pressure at the liquid exit). In this work, we consider only the domain in the dashed box, and do not consider the entrance or exit effects in the liquid or the gas. The local coordinate frame, based on the channel, is also shown.

$$\nabla \cdot \mathbf{u}^{(i)} = 0, \tag{2}$$

$$Re_l \frac{\rho_i^*}{\rho_1^*}\left[\frac{\partial \mathbf{u}^{(i)}}{\partial t} + \mathbf{u}^{(i)} \cdot \nabla \mathbf{u}^{(i)}\right] = -\nabla p^{(i)} + \frac{\rho_i^*}{\rho_1^*}\hat{\mathbf{g}} + \frac{\mu_i^*}{\mu_1^*}\nabla^2 \mathbf{u}^{(i)}, \tag{3}$$

where $Re_l = gd^3/\nu_1^{*2}$ is the Reynolds number for lower fluid, $\hat{\mathbf{g}}$ is the unit vector in the direction of gravity, and velocities are $\mathbf{u}^{(i)} = (u^{(i)}, w^{(i)})$.

The boundary conditions on the channel walls become: $\mathbf{u}^{(1)} = 0$ on z=0 and $\mathbf{u}^{(2)} = 0$ on $z = 1$. The conditions (1) at $z = h(x, t)$ become:

$$[\mathbf{n} \cdot \mathbf{T} \cdot \mathbf{n}] = \sigma\kappa, \qquad [\mathbf{t} \cdot \mathbf{T} \cdot \mathbf{n}] = 0, \qquad [\mathbf{u} \cdot \mathbf{n}] = 0, \qquad [\mathbf{u} \cdot \mathbf{t}] = 0, \qquad h_t + uh_x - w = 0. \tag{4}$$

where $\sigma = \sigma^*/\rho_1 d^2 g$.

Since we are interested in gas–liquid systems, the density and dynamic viscosity ratios are small. Following the case of air-water (under standard conditions: $\rho_2^*/\rho_1^* = 8 \times 10^{-4}$, $\mu_2^*/\mu_1^* = 2 \times 10^{-2}$), we assume that $\overline{\rho} = \rho_2^*/\rho_1^*$ is of the order ϵ^2 and $\overline{\mu} = \mu_2^*/\mu_1^*$ is of the order ϵ, where ϵ is an aspect ratio of channel thickness to a characteristic channel length, i.e. $\overline{\rho} = \epsilon^2\rho$, $\overline{\mu} = \epsilon\mu$, and ρ, μ are $O(1)$. This distinguished limit allows us to capture the dominant physical effects in this system, while simplifying the analysis considerably. For an air-water system, this scaling is consistent with experiments performed in the channels several hundred microns high (see, e.g. Pettigrew et al. [20]).

In terms of the Reynolds numbers for the liquid and the gas, if U_l is the characteristic velocity of the liquid, and U_g is the characteristic velocity of the gas, then the ratio of the liquid Reynolds number to the gas Reynolds number

is given by:

$$\frac{Re_l}{Re_g} = \frac{\mathrm{d}\,U_l/\nu_1^*}{\mathrm{d}\,U_g/\nu_2^*} = \frac{\nu_2^*}{\nu_1^*}\frac{U_l}{U_g} = \frac{1}{\epsilon}\frac{U_l}{U_g}.$$

Therefore, the tangential gas velocity scale is $O(U_l/\epsilon)$ for Re_g, $Re_l = O(1)$.

Next, we assume that changes of the flow occur on spatial scale that is much longer than the channel thickness. Therefore, we use scaled variables $\xi = \epsilon x$ and $\zeta = z$. The kinematic boundary condition (4) then requires rescaling of time as $\tau = \epsilon t$.

Assume a regular perturbation expansion for u in ϵ:

$$u^{(1)}(\xi, \zeta, \tau) = u_0^{(1)}(\xi, \zeta, \tau) + \epsilon u_1^{(1)}(\xi, \zeta, \tau) + \cdots$$

and then from the continuity Eq. (2) it follows that:

$$w^{(1)}(\xi, \zeta, \tau) = \epsilon \left\{ w_0^{(1)}(\xi, \zeta, \tau) + \epsilon w_1^{(1)}(\xi, \zeta, \tau) + \cdots \right\}.$$

For the second fluid, since the viscosity ratio is small ($O(\epsilon)$), and the density ratio is even smaller ($O(\epsilon^2)$), we can allow for the gas velocities to be large, $O(1/\epsilon)$, and hence we expand:

$$u^{(2)}(\xi, \zeta, \tau) = \frac{1}{\epsilon} \left\{ u_0^{(2)}(\xi, \zeta, \tau) + \epsilon u_1^{(2)}(\xi, \zeta, \tau) + \cdots \right\}.$$

From the continuity Eq. (2):

$$w^{(2)}(\xi, \zeta, \tau) = w_0^{(2)}(\xi, \zeta, \tau) + \epsilon w_1^{(2)}(\xi, \zeta, \tau) + \cdots$$

Since the system is driven by a pressure gradient and possibly gravity, we expect from balancing terms in (3) that the downstream pressure gradients will be of unit order:

$$p^{(i)}(\xi, \zeta, \tau) = \frac{1}{\epsilon} \left\{ p_0^{(i)}(\xi, \zeta, \tau) + \epsilon p_1^{(i)}(\xi, \zeta, \tau) + \cdots \right\}, \qquad i = 1, 2.$$

We assume large surface tension and define the unit-order parameter $S = \epsilon^2\sigma$. Next step is to asymptotically expand the governing equations in powers of ϵ. Following the procedure in [23], we expand the governing equations in powers of ϵ and obtain a sequence of problems whose solutions depend on the solution of the coupled nonlinear evolution equation and the pressure gradient equation:

$$h_\tau + A_1(h, p_{0\xi})h_\xi + \epsilon \left[S\frac{h^3}{3}h_{\xi\xi\xi} + A_2(h, p_{0\xi}) - \frac{h^3}{3}\cos\beta h_\xi \right]_\xi = 0, \qquad [p_{0\xi}(1-h)^3]_\xi = 0, \tag{5}$$

where

$$A_1(h, p_{0\xi}) = h^2 \sin\beta - \frac{h(h+1)}{2(1-h)}p_{0\xi},$$

$$A_2(h, p_{0\xi}) = \frac{\mu h^3 p_{0\xi}}{4(1-h)} + \frac{\mu h^4}{4(h-1)}\sin\beta + \frac{\mu h^2(h+3)}{(1-h)^3}\left[\gamma - \frac{h^2(h+3)}{12}\sin\beta - \frac{h(h-1)}{4}p_{0\xi}\right].$$

and

$$\gamma = \int_0^{\xi} \frac{h(h+1)h_{\hat{\xi}} p_{0\hat{\xi}}}{2(1-h)} \mathrm{d}\hat{\xi}.$$

The second term in the evolution equation corresponds to advection effects and consists of two sub-terms: the first one describes wave propagation and steepening, and the second the influence of pressure gradient. The third, fourth and fifth terms in the evolution equation describe mean surface tension, correction to advection, and hydrostatic effects. These equations are derived assuming $Re_l = 0$; we note that very similar results are obtained for $O(1)$ liquid Reynolds numbers.

The asymptotic analysis proposed above breaks down if the interfacial height h gets too close to the upper wall. We see this when the leading-order terms in A_1 and ϵA_2 become comparable, where

$$\frac{1}{(1-h)^3} \sim \frac{\epsilon}{(1-h)^6},$$

for the constant gas volumetric flow rate condition. Hence our theory breaks down for values of interfacial height where $1 - h \sim \epsilon^{1/3}$.

Intergrating (5) with respect to ξ gives:

$$p_{0\xi} = \frac{\Phi(\tau)}{(1-h)^3},$$

where function $\Phi(\tau)$ depends on the conditions which are imposed on the flow. Note that pressure gradient is not a function of ζ.

One possible condition is to prescribe the gas volumetric flow rate $q(\tau)$:

$$q(\tau) = \int_h^1 u_0^{(2)} \mathrm{d}\zeta.$$

After substituting of the appropriate expression for tangential gas velocity we obtain:

$$q(\tau) = -\frac{(1-h)^3}{12\mu} p_{0\xi}, \qquad \Phi_1(\tau) = -12\mu q(\tau). \tag{6}$$

Thus, if q is held fixed, the pressure gradient is determined by the interfacial deflection $h(\xi, \tau)$. To close the problem, we prescribe boundary conditions for evolution Eq. (5).

A second possibility is to define pressure drop $\Delta P = p_0(0) - p_0(1)$ and then:

$$\Phi_2(\tau) = -\frac{\Delta P}{\int_0^1 \mathrm{d}\xi/(1-h)^3}. \tag{7}$$

In this case, the gas volumetric flow rate is determined by the global effect of the interfacial height. In our previous study [23], condition (7) provides the solution of the pressure gradient equation. In addition, the prescribed boundary conditions for $h(\xi, \tau)$ fully determines the problem.

A third possibility of formulating this problem is to prescribe the liquid flow rate (Q_l) and pressure drop (ΔP) over the length of the channel. These are more physical boundary conditions because the experiments (see [1]) are typically performed using constant liquid flow rate and constant pressure drop formulation. We see below that Q_l

and ΔP can not be prescribed independently. We define liquid flow rate Q_l by:

$$Q_l = \int_0^h u_0^{(1)} \mathrm{d}\zeta.$$

After substituting the corresponding expression for tangential velocity of the lower fluid we obtain

$$Q_l = -\frac{p_{0\xi}(h+3)}{12} + \frac{h^3}{3}\sin\beta. \tag{8}$$

To obtain a prescribed pressure drop ΔP we integrate (8):

$$\Delta P = 4\int_0^1 \frac{3Q_l - h^3\,\sin\beta}{h+3}\mathrm{d}\xi. \tag{9}$$

One approach to satisfying (8) for a given Q_l and ΔP, and to avoid illposedness, is to allow the average interfacial height (the averaged integral of the interfacial height $h(\xi, \tau)$) to vary in time. Eq. (9) is the required relation which Q_l and ΔP need to satisfy.

In this paper, we consider either that the gas volumetric flow rate and the interfacial heights at the inlet and exit of the channel are fixed and $p_{o\xi}$ is found explicitly in terms of $h(\xi, \tau)$ or that both Q_l and ΔP are prescribed. We will discuss the differences between these two scenarios further. For simplicity of notation, we return to using x for the downstream coordinate, instead of ξ and to t for the time variable instead of τ.

3. Numerical simulation

Before outlining the numerical method we discuss the imposed boundary conditions. For simplicity in this work, we chose not to include the edge effects of the entrance or exit region of the fluid layer (see Fig. 1). Instead, we simulate a region of the channel in which the fluid heights at $x = 0$ (which we call the inlet) is prescribed to be h_-, while the height at $x = L$ (which we call the exit) is held fixed at h_+. Admittedly, these conditions may not be the appropriate conditions found in experiment, but they do provide a starting point from which the dynamics of the system can be understood. The results obtained using these conditions will also provide some insight into so-called contact line problems where there is a moving fluid front in the domain. These problems are often modeled by assuming presence of a precursor film, therefore effectively removing the contact line itself. Although the value of h_+ that we use is not very small (typically $h_+ = 0.1$), there is a reason to expect that at least some basic physical understanding can be reached since the precursor films of this thickness have been used extensively in the literature to model successfully the macroscopic flow features in the flows involving contact lines. We close the system of differential equations assuming that interface remains flat at the boundaries: $h_x(x = 0) = 0$ and $h_x(x = L) = 0$. For the flow driven by prescribed Q_l and ΔP we allow the interfacial height at the inlet and outlet of the channel to adjust (as discussed above), i.e. $h_x(x = 0) = h_{xxx}(x = 0) = 0$ and $h_x(x = L) = h_{xxx}(x = L) = 0$.

The numerical method that we use is based on finite difference discretization method with N equally spaced grid points. Time discretization is performed by a Crank–Nicholson scheme. The resulting nonlinear algebraic system of N equations is solved using iterative Newton–Kantorovich's method. Boundary conditions are implemented using ghost points. For more details we refer to Diez and Kondic [8] and to [23].

We proceed with numerical comparison of the interfacial profiles resulted in the flows driven by either constant gas volumetric flow rate, or by prescribed liquid flow rate and gas pressure drop.

3.1. Constant gas volumetric flow rate

The case of constant gas volumetric flow rate is discussed in [23]. Now we briefly summarize the results of that work and relate them to earlier results [4] on single phase Marangoni flows.

In [4] the case of a thin liquid film under the influence of gravity and thermocapillary forces is investigated. The evolution equation found in that work is of the form

$$h_t + f'(h)h_x + \{C(h)h_{xxx}\}_x = 0,$$

where $f(h)$ is the flux function. For this system, $f(h) = h^2 - h^3$. Using entropy-entropy flux pairs it was shown that several distinct solution régimes exist, distinguished by the value of the upstream value $h = h_-$. For a given height h_1, if $h_+ < h_- < h_1$, one obtains unique traveling-wave solution characterized by the capillary ridge (Lax shock). If $h_1 < h_- < h_2$, then multiple stable solutions are found; the Lax shock traveling wave, and a double-shock structure whose maximum height remains fixed, but the capillary ridge region broadens in time. For $h_2 < h_- < h_{UC}$, the Lax shock solution loses stability, and only the double-shock structure is seen. For $h_{UC} < h_-$, a combination of a rarefaction wave and an undercompressive shock is seen.

In [23] we apply a similar analysis to find regions in the (h_-, h_+) plane which are compatible to traveling wave solutions for the two-layer flow system. Using the same concept of entropy-entropy flux pair [4], we analytically find regions where the traveling-wave solutions may exist. Fig. 2 shows this region bounded by solid curve for particular values of $q = -0.004$, $S = 3$, $Re_l = 0$, $\epsilon = 0.01$, $\mu = \rho = 1$, $\beta = \pi/2$. The symbols in this figure correspond to stability transitions (described below) from the Lax shock régime to the bistability régime to the double-shock régime, and the combinations of rarefaction waves and undercompressive shocks. Note that a complete proof of the uniqueness of solutions in any of these régimes could not be found, but from our numerical study, we suspect that this organizational structure, which is similar to the one in single phase flow, describes the two-layer case as well. In the two-layer case, the flux function f for a constant gas volumetric flow rate is given by:

$$f(h) = \frac{h^3}{3}\sin\beta + \mu q\frac{6h^2 - 3h + 1}{(1-h)^3} + \epsilon\left[-\frac{12\mu^2 q h^3}{(1-h)^5} - \frac{\mu\sin\beta h^4(h^2+3)}{3(1-h)^3} + \frac{\mu h^2(h+3)}{(1-h)^3}\gamma\right].$$

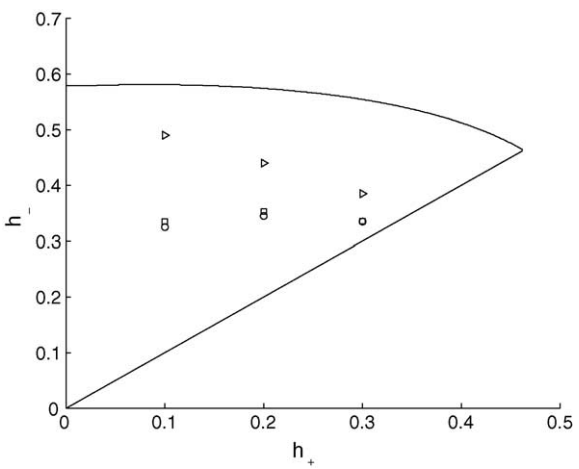

Fig. 2. Regions for admissible traveling shock solutions for $q = -0.004$, $\epsilon = 0.01$, $\beta = \pi/2$, $\rho = \mu = 1$, $S = 3$, $Re_l = 0$. The circles denote h_1, diamonds h_2, and light right triangles denote the combination of rarefaction and undercompressive waves.

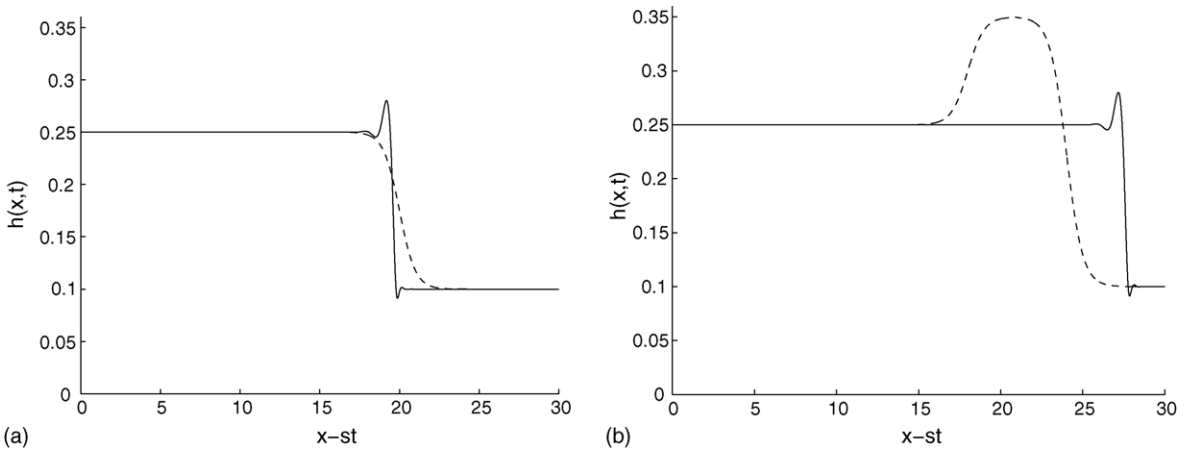

Fig. 3. Interfacial profile with unique Lax shock for $h_- = 0.25$, $h_+ = 0.1$, $q = -0.001$, $S = 3$, $Re_l = 0$, $\epsilon = 0.01$, $\mu = \rho = 1$, $\beta = \pi/2$. Dashed line shows the initial condition and the solid one shows the steady (in the moving frame) Lax shock solution, (a) using the initial condition given by (11), (b) using the initial condition (12).

In the first region, $h_+ < h_- < h_1$, for given h_+, the solution of (5) is always observed to evolve to a unique capillary shock profile connecting the states h_- and h_+. Fig. 3 shows the solutions, computed in the reference frame moving with phase speed its,

$$s(h_-, h_+) = \frac{f(h_-) - f(h_+)}{h_- - h_+}, \tag{10}$$

and two initial profiles

$$h_0(x) = [\tan h(-x + 20) + 1]\frac{h_- - h_+}{2} + h_+ \tag{11}$$

and

$$h_0(x) = \begin{cases} \frac{h_+ - h_-}{2} \tan h(x - 18) + \frac{h_+ + h_-}{2}; & \text{if} \quad x < 21 \\ -\frac{h_+ - h_-}{2} \tan h(x - 24) + \frac{h_+ + h_-}{2}; & \text{if} \quad x > 21 \end{cases} \tag{12}$$

connecting the states h_- and h_+.

Interfacial profiles settle down to a steady traveling wave solution, which is independent of the considered initial condition.

For h_- in the range $h_1 < h_- < h_2$, there are multiple capillary shock profiles connecting the same two left (h_-) and right (h_+) states. Fig. 4 shows several solutions connecting $h_+ = 0.1$ and $h_- = 0.4$. Depending on the initial condition we obtain either the single Lax shock or double shock structure, evolving into the undercompressive shock (leading shock) and Lax shock (trailing shock).

For h_- in the range $h_2 < h_- < h_{UC}$, there are no capillary shock profiles joining h_- and h_+. All considered initial conditions converge to a solution with the same double shock structure. Fig. 5a illustrates these results for the case $h_- = 0.5$. [2] This double shock wave structure persists for $h_- < h_{UC}$. For $h_- > h_{UC}$, Fig. 5b shows the solution at time $t = 100$; this solution involves the combination of rarefaction wave and undercompressive shock.

Next, we turn out attention to the flow driven by prescribed liquid flow rate and pressure drop.

[2] Note that h_- used here is close to the value at which the asymptotic analysis is no longer strictly valid. More work is needed to understand this regime in detail.

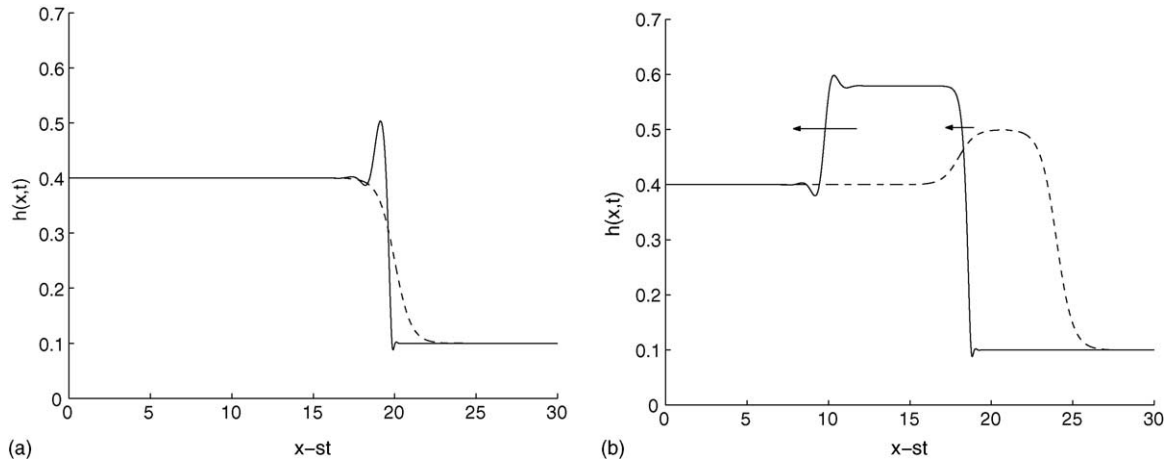

Fig. 4. Interfacial profile resulting in steady Lax shock (in moving frame) for $h_- = 0.4$ and other parameters as in Fig. 3 (a) using initial condition given by (11), (b) using the initial condition given by (12). Note that in the latter case the double shock structure is no longer steady in the sense that it moves to the left (in the direction of the arrows) with capillary ridge broadening in width.

3.2. Constant liquid flow rate and constant pressure drop

We proceed to examine four regions obtained for the case of constant gas volumetric flow rate, and investigate whether different imposed boundary conditions for the pressure and interfacial height lead to a different interfacial dynamics. All cases discussed below use $Q_l = 0.01$, $h_+ = 0.1$, $\rho = \mu = 1$, $S = 3$, $Re_l = 0$, $\beta = \pi/2$ and prescribed pressure drop ΔP. Fixing the liquid flow rate along with the initial condition determines the pressure drop which we keep fixed from now on. We note that we have carried out the computations with inertial effects included as well. We find that as long as $Re_l = O(1)$, the results are practically indistinguishable from the ones presented here [23].

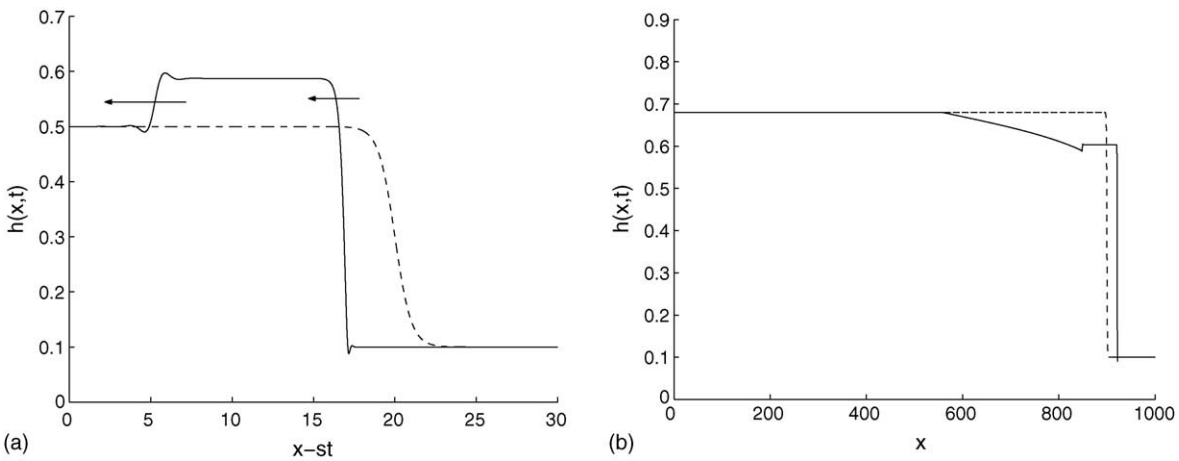

Fig. 5. (a) Undercompressive double shock structure for $\tau = 300$, $h_- = 0.5$ and other parameters as in Fig. 3, with the initial condition given by (11). The direction of propagation is indicated by the arrows. (b) Interfacial profile at $t = 0$ (dashed line) and $t = 400$ (solid), for $h_- = 0.68$ and other parameters as in Fig. 3.

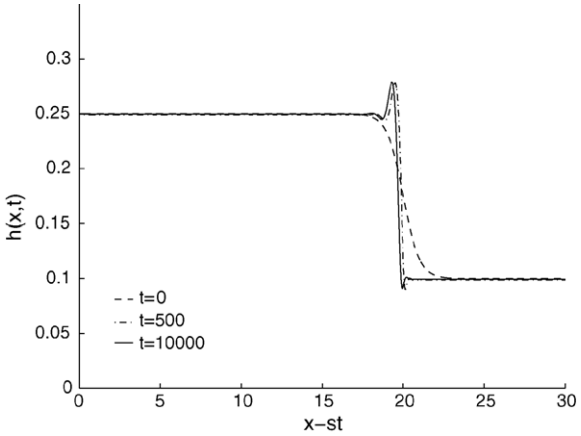

Fig. 6. Interfacial profile with Lax shock for $Q_l = 0.01$, $\Delta P = 0.735$, $Re_l = 0$, $\epsilon = 0.01$, $\beta = \pi/2$, $\rho = \mu = 1$, $S = 3$, $h_- = 0.25$, $h_+ = 0.1$. Solid line shows the initial condition, dashed and dashed-dot lines show Lax shock solution. Here we use the initial condition given by (11).

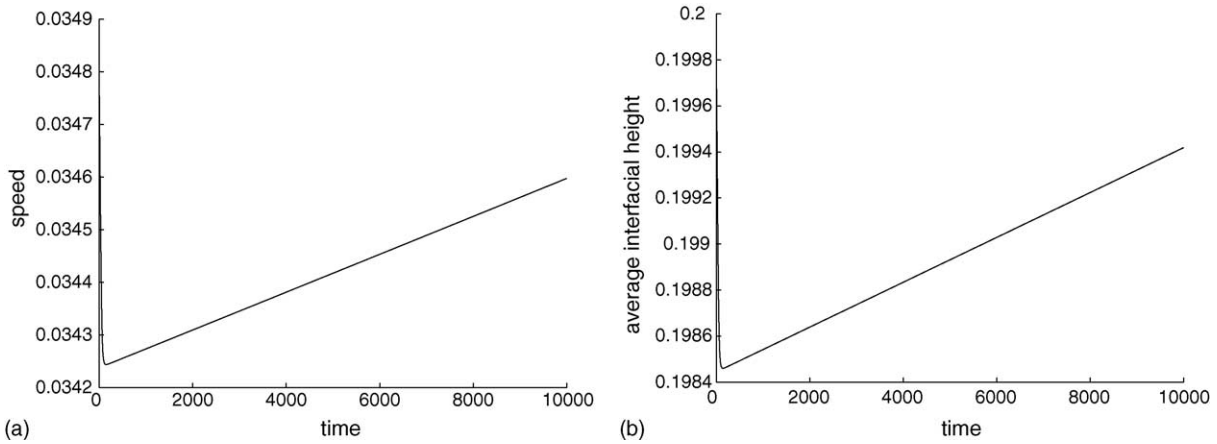

Fig. 7. Speed profile (a) and average interfacial height (b) for Lax shock for parameters as in Fig. 6.

3.2.1. Case 1: weak Lax shock

Fig. 6 shows the initial interfacial profile (solid line) evolving into the Lax shock (dashed line). In contrary to Fig. 3 where the profile reaches its steady state, we observe that Lax shock is no longer steady. Since this may not be obvious from Fig. 6 we plot the phase speed s given by (10) in Fig. 7a. This figure shows that s does not saturate to a constant value. Moreover, the average interfacial height (calculated as as integral of $h(x, t)$ over the length of the channel) increases in time (Fig. 7b). Both graphs therefore show that Lax shock does not settle to unique steady profile. Thus, in this case we observe classical Lax shock which is unsteady.

3.2.2. Case 2: ($h_1 < h_- < h_2$)—multiple Lax shock

Next, we proceed with simulations for h_- corresponding to multiple capillary shock profiles connecting the left (h_-) and right (h_+) states. Fig. 8 shows several solutions connecting $h_+ = 0.1$ and $h_- = 0.431$. [3] Depending

[3] Here, we change the value of h_- compared to the one used in Fig. 4, since the region corresponding to Case 3.2.2 is different due to the application of the different constraints at $O(\epsilon)$.

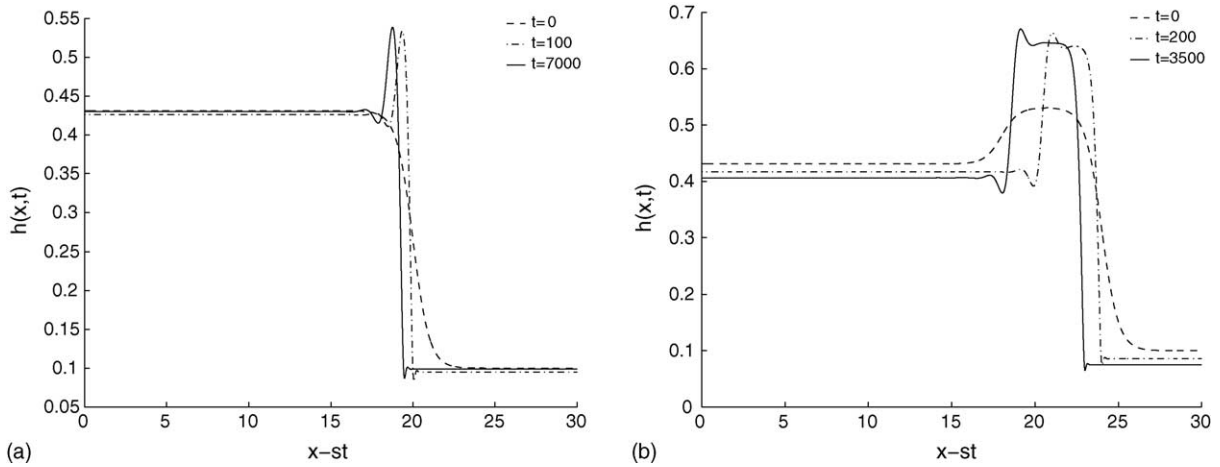

Fig. 8. Interfacial profiles for $h_- = 0.431$, ΔP to be specified below and other parameters as in Fig. 6. (a) Weak Lax shock (in moving frame), using the initial condition (dashed line) given by (11) for $\Delta P = -0.74$. (b) Double shock wave profiles for $\Delta P = -1.54$ using the initial condition (dashed line) given by (12). Note that this double-shock structure is no longer steady in the sense that it moves to the left with the broadening capillary ridge before its maximum height approaches the constant value (solid line) near $t = 3500$.

whether the initial conditions (11) or (12) are used, we obtain either the single Lax shock or double shock structure, evolving into the undercompressive shock (leading shock) and Lax shock (trailing shock). Similarly to Case 3.2.1, Lax shock profile is no longer steady, as also shown in Fig. 9a. However, the double shock structure reaches its steady state (Fig. 9b), meaning that the maximum height of the interface reaches the constant value, equal to 0.67. Future work will show whether this behavior persists for all h_- in this range when condition (12) is used.

3.2.3. Case 3: ($h_2 < h_- < h_{UC}$)—undercompressive double shock structure

For h_- in this range, there are no capillary shock profiles joining h_- and h_+. All initial conditions converge to a solution with the same double shock structure. Fig. 10a illustrates this behavior for the case $h_- = 0.5$. The solution at the later time is characterized by the presence of two shocks. We observe here that the maximum interfacial height of double shock wave structure grows in time, in contrast to the results shown in Fig. 5a. Fig. 10b presents

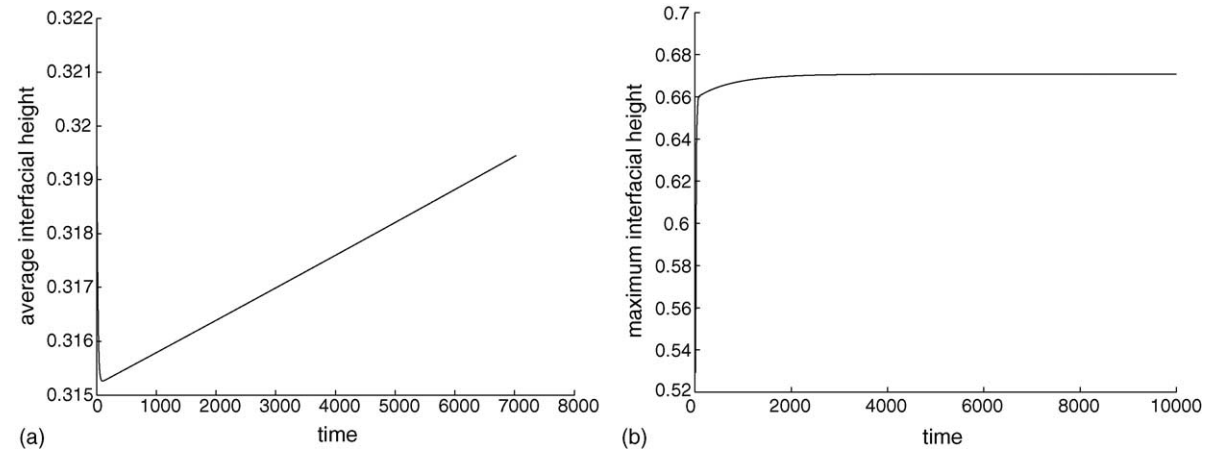

Fig. 9. (a) Change of the average interfacial height for the parameters from Fig. 8a. (b) Maximum interfacial height for parameters from Fig. 8b.

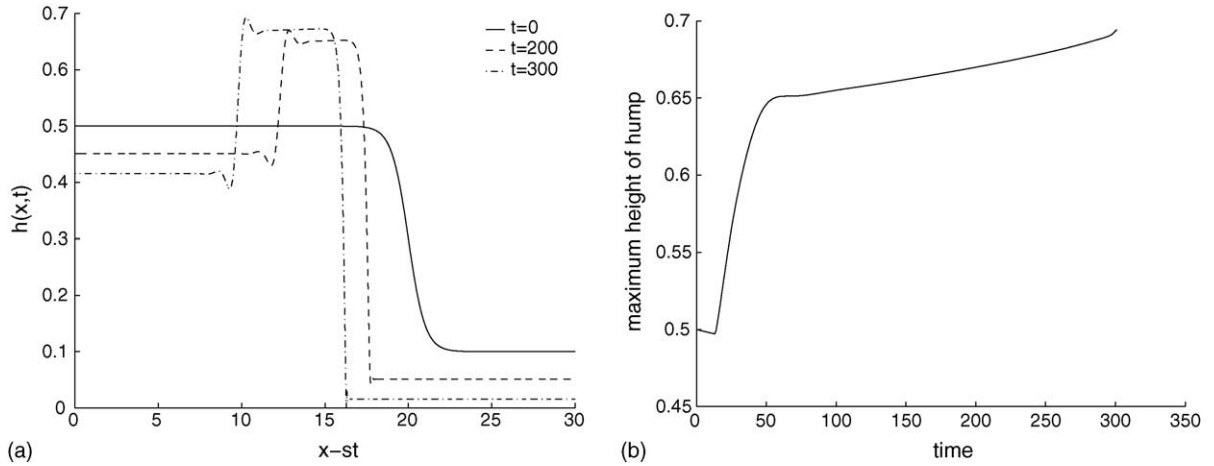

Fig. 10. (a) Interfacial profile with undercompressive shock for $\Delta P = -1.72$, $h_- = 0.5$ and other parameters as in Fig. 6. We use the initial condition given by (11). (b) Change of the maximum height of undercompressive shock in time.

growth of maximum of the interfacial height. We note that in this case both the thickness of the precursor film and h_- decrease, corresponding to the fact that the average interfacial height decreases in time.

3.2.4. Case 4: ($h_- > h_{UC}$)—rarefaction-undercompressive shock

For $h_- > h_{UC}$ we obtain a two-wave structure in which the slower wave is a rarefaction wave solution and the other is undercompressive shock. We use $h_- = 0.68$ and the initial condition

$$h_0(x) = [\tan h(-x + 925) + 1]\frac{h_- - h_+}{2} + h_+.$$

For this case simulations are performed in the fixed frame in order to capture two-wave structure. Fig. 11 shows a combination of rarefaction wave and undercompressive shock. We see similar features as in Fig. 5b, with the main difference that here the maximum of the interfacial height grows in time, similarly to Cases 1–3.

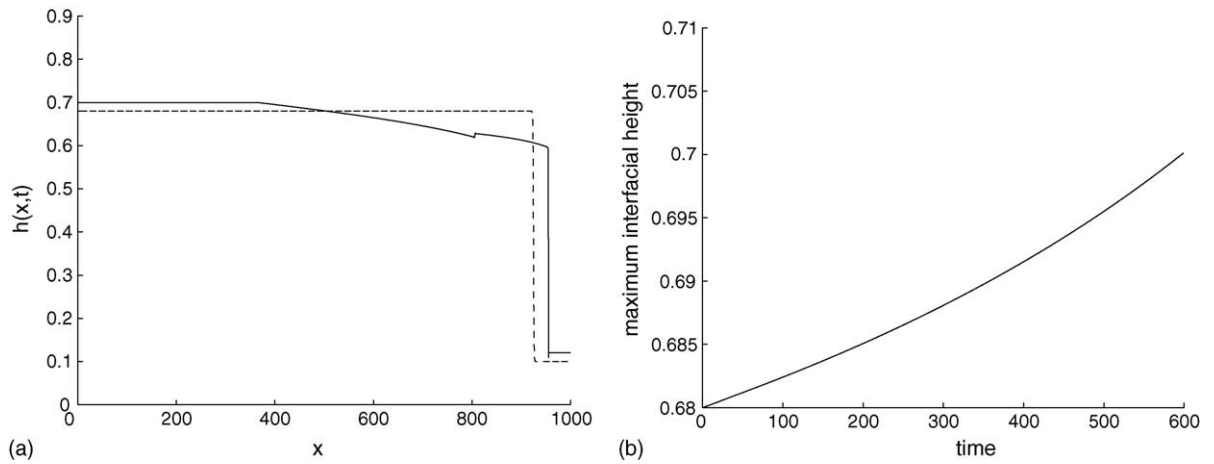

Fig. 11. (a) Interfacial profiles for $h_- = 0.68$, $\Delta P = -282.97$ and other parameters as in Fig. 6. Dashed line is initial condition and solid line shows the solution at time $t = 600$. (b) Maximum of interfacial height.

4. Conclusions

In this work, we have investigated numerically the nonlinear evolution of the interface between two incompressible immiscible fluids in an inclined channel. Motivated by air-water systems, through a lubrication approximation, we derive a system of nonlinear evolution equations that govern the interfacial motion between the two fluids and the leading-order pressure contribution. The lubrication approach includes the inertial effects of the liquid layer and steady Bernoulli pressure effects in the gas layer.

We consider two different forcing scenarios. The first, where the gas volumetric flow rate is fixed, results in a standard lubrication approximation, and the interfacial dynamics depends only on local variations of the interfacial shape. The second, where the liquid flow rate and gas pressure difference over the length of the channel are fixed, results in an additional constraint on flow. In each of these cases, we find that the undercompressive shock paradigm found in Marangoni-driven fluid layers is applicable in the counter-current flow régime. We obtain that small differences in the upstream and downstream interfacial height results in the formation of Lax shocks. Larger differences in the upstream and downstream heights result in bistability among multiple Lax shocks. Increasing this differential still further results in the formation of undercompressive shocks and finally the formation of rarefaction waves. In the case of the flow driven by constant pressure drop and liquid flow rate, we observe growth of either maximum or average interfacial height. This is especially interesting for the case of undercompressive shock height h_{UC}. In this régime it is more likely that the advection and inertial effects (comparable to surface-tension effects) may result in capturing the final state of the transient related to a flooding scenario—the size of the hump actually reaches the upper channel wall.

Acknowledgments

B.S.T., T.M.S. acknowledge supported from NSF grant no. DMS-9971383, and L.K. partial support from NSF grant no. INT-0122911.

References

[1] S.G. Bankoff, S.C. Lee, Multiphase science and technology, in: G.F. Hewitt, J.M. Delhaye, N. Zuber (Eds.), A Critical Review of the Flooding Literature, Hemisphere, 1986.
[3] A.L. Bertozzi, A. Munch, X. Fanton, A.M. Cazabat, Contact line stability and “undercompressive shocks” in driven thin film flow, Phys. Rev. Lett. 81 (1998) 5169–5172.
[4] A.L. Bertozzi, A. Munch, M. Shearer, Undercompressive shocks in thin film flows, Physica D 134 (1999) 431–464.
[5] W.S. Bousman, J.B. McQuillen, L.C. Witte, Gas–liquid flow patterns in microgravity: effects of tube diameter, liquid viscosity and surface tension, Int. J. Multiphase Flow 22 (1996) 1035–1053.
[6] P. Carles, A.M. Cazabat, The thickness of surface-tension-gradient-driven spreading films, J. Colloid Interface Sci. 157 (1993) 196–201.
[7] H.-C. Chang, Nonlinear waves on liquid film surfaces. Part I: Flooding in a vertical tube, Chem. Eng. Sci. 41 (1986) 2463–2476.
[8] J.A. Diez, L. Kondic, Computing three dimensional thin film flows including contact lines, J. Compd. Phys. 183 (2002) 274–306.
[9] R. Duenckel, Improved Fracture Conductivity Brings Value to Hydraulic Fracturing, Am. Oil Gas Report (2002).
[10] A.E. Dukler, J.A. Fabre, J.B. McQuillen, R. Vernon, Gas liquid flow at microgravity conditions: flow patterns and their transitions, Int. J. Multiphase Flow 14 (1988) 389–400.
[11] A.E. Dukler, L. Smith, Two-phase interactions in countercurrent flow: studies of the flooding mechanism, NUREG/CR-0617 Nuclear Regulatory Commision Washington, DC, 1979.
[12] A.C. Fowler, P.E. Lisseter, Flooding and flow reversal in annular two-phase flows, SIAM J. Appl. Math. 52 (1992) 15–33.
[15] A. Kluwick, E.A. Cox, S. Scheichl, Non-classical kinematic shocks in suspensions of particles in fluids, Acta Mechanica 144 (2000) 197–210.
[16] C. Kouris, J. Tsamopoulos, Dynamics of the axisymmetric core-annular flow. II. The less viscous fluid in the core, saw tooth waves, Phys. Fluids 13 (2002) 1011–1029.

[17] V. Ludviksson, E.N. Lightfoot, The dynamics of thin liquid films in the presence of surface-tension gradients, AIChE J. 17 (1971) 1166–1173.
[18] D. Marchesin, B.J. Plohr, Wave structure in WAG recovery, SPE J. 6 (2001) 209–219.
[19] G. Moritis, Flow assurance challenges production from deeper water, Oil Gas J. 99 (2001) 66–69.
[20] K. Pettigrew, J. Kirshberg, K. Yerkes, D. Trebotich, D. Liepmann, Performance of a MEMS based micro capillary pumped loop for chip-level temperature control, IEEE (2001) 427–430.
[21] M. Schneemilch, A.M. Cazabat, Wetting films in thermal gradients, Langmuir 16 (2000) 8796–8801.
[22] M. Schneemilch, A.M. Cazabat, Shock separation in wetting films driven by thermal gradients, Langmuir 16 (2000) 9850–9856.
[23] T. Segin, B.S. Tilley, L. Kondic, On undercompressive shocks and flooding in countercurrent two-layer flows, J. Fluid Mech. 532 (2005) 217–242.
[24] B.S. Tilley, S.H. Davis, S.G. Bankoff, Linear stability theory of two-layer fluid flow in an inclined channel, Phys. Fluids A 6 (1994) 3906–3922.
[25] B.S. Tilley, S.H. Davis, S.G. Bankoff, Nonlinear long-wave stability of superposed fluids in an inclined channel, J. Fluid Mech. 277 (1994) 55–83.
[26] C.-S. Yih, Instability due to viscosity stratification, J. Fluid Mech. 27 (1967) 337–352.